Spatial and Temporal Characteristics of the Submesoscale Energetics in the Gulf of Mexico

YANG YANG,[a,b,c] JAMES C. MCWILLIAMS,[a,d] X. SAN LIANG,[b] HONG ZHANG,[e] ROBERT H. WEISBERG,[c] YONGGANG LIU,[c] AND DIMITRIS MENEMENLIS[e]

[a] *School of Marine Sciences, Nanjing University of Information Science and Technology, Nanjing, China*
[b] *Center for Ocean-Atmosphere Dynamical Studies, Nanjing University of Information Science and Technology, Nanjing, China,*
[c] *College of Marine Science, University of South Florida, St. Petersburg, Florida*
[d] *Department of Atmospheric and Oceanic Sciences, University of California, Los Angeles, Los Angeles, California*
[e] *Jet Propulsion Laboratory, California Institute of Technology, Pasadena, California*

(Manuscript received 9 October 2020, in final form 15 November 2020)

ABSTRACT: The submesoscale energetics of the eastern Gulf of Mexico (GoM) are diagnosed using outputs from a 1/48° MITgcm simulation. Employed is a recently developed, localized multiscale energetics formalism with three temporal-scale ranges (or scale windows), namely, a background flow window, a mesoscale window, and a submesoscale window. It is found that the energy cascades are highly inhomogeneous in space. Over the eastern continental slope of the Campeche Bank, the submesoscale eddies are generated via barotropic instability, with forward cascades of kinetic energy (KE) following a weak seasonal variation. In the deep basin of the eastern GoM, the submesoscale KE exhibits a seasonal cycle, peaking in winter, maintained via baroclinic instability, with forward available potential energy (APE) cascades in the mixed layer, followed by a strong buoyancy conversion. A spatially coherent pool of inverse KE cascade is found to extract energy from the submesoscale KE reservoir in this region to replenish the background flow. The northern GoM features the strongest submesoscale signals with a similar seasonality as seen in the deep basin. The dominant source for the submesoscale KE during winter is from buoyancy conversion and also from the forward KE cascades from mesoscale processes. To maintain the balance, the excess submesoscale KE must be dissipated by smaller-scale processes via a forward cascade, implying a direct route to finescale dissipation. Our results highlight that the role of submesoscale turbulence in the ocean energy cycle is region and time dependent.

KEYWORDS: Eddies; Frontogenesis/frontolysis; Instability; Small scale processes

1. Introduction

Submesoscale currents with a horizontal scale of $O(0.1–50)$ km and a time scale of $O(1)$ days are ubiquitous in the ocean. They occur preferentially near the surface of the ocean in the form of fronts, filaments and small-scale eddies, characterized by large variances of vertical velocity and vorticity (Thomas et al. 2013; McWilliams 2016). Submesoscale processes can be generated through various mechanisms such as mixed layer instabilities (e.g., Boccaletti et al. 2007; Fox-Kemper et al. 2008; Capet et al. 2016; Thompson et al. 2016), frontogenesis (e.g., Hoskins 1982; McWilliams 2017; Barkan et al. 2017), and flow–topography interactions (e.g., Gula et al. 2016; Srinivasan et al. 2017). They are important not only because of their ability to modify the upper-ocean stratification (Boccaletti et al. 2007) and the vertical redistribution of heat and material tracers (e.g., Klein and Lapeyre 2009; Lévy et al. 2012; Su et al. 2018; Uchida et al. 2019) but also because they may provide a dynamical route to microscale dissipation in the global-ocean energy cycle (D'Asaro et al. 2011; Molemaker et al. 2010; Brüggemann and Eden 2015).

As is well known in turbulence theory, three-dimensional (3D) small-scale isotropic turbulence is characterized by a forward cascade of kinetic energy (KE) to smaller scales where it is finally dissipated on molecular scales (Kolmogorov et al. 1991). In contrast, the KE in a quasigeostrophically balanced flow (such as oceanic mesoscale eddies) tends to be transferred back to larger scales through inverse cascade and thus is inhibited from further transferring KE to smaller scales (Charney 1971; Salmon 1980). With intermediate space and time scales, the submesoscale currents have been recognized as an efficient conduit for KE to forward-cascade toward dissipation scales (Müller et al. 2005; McWilliams 2016). For example, by probing into the spectral KE balance in a high-resolution simulation, Capet et al. (2008b) found a significant forward cascade of KE in the submesoscale range associated with unbalanced ageostrophic flows. Such a direct energy route to dissipation, which occurs preferentially at small scales near the ocean surface, is confirmed in a vast number of follow-up studies using observational measurements and numerical simulations (e.g., Molemaker et al. 2010; D'Asaro et al. 2011; Skyllingstad and Samelson 2012; Barkan et al. 2015; Brüggemann and Eden 2015; Balwada et al. 2016; Poje et al. 2017). Analogous to quasigeostrophic turbulence, however, submesoscale turbulence is also found to energize larger-scale motions through inverse KE cascades (Klein et al. 2008; Qiu et al. 2014; Sasaki et al. 2014; Capet et al. 2016; Dong et al. 2020; Schubert et al. 2020). The bidirectional behavior of the KE cascades indicates the complex nature of multiscale interactions in the submesoscale flow regime, which is likely to exhibit distinct features at different locations and times.

In this study, we employ a recently developed multiscale energetics analysis and canonical transfer theory (Liang 2016)

Corresponding author: X. S. Liang, sanliang@courant.nyu.edu

DOI: 10.1175/JPO-D-20-0247.1

to analyze the scale interactions and energetics associated with submesoscale currents in the eastern Gulf of Mexico (GoM), using output from a global, 1/48° ocean simulation carried out using the Massachusetts Institute of Technology general circulation model (MITgcm). Based on a new analysis apparatus, namely, multiscale window transform (MWT; Liang and Anderson 2007), the energetics framework of the present study is carried out in a four-dimensional fashion (i.e., localized in both space and time), thus allowing for an investigation of the spatiotemporal structures of the energetic processes. Since the 2010 *Deepwater Horizon* incident, there have been continuing efforts to understand mesoscale and submesoscale processes in the GoM. In particular, a large number of drifters were deployed as part of the Grand Lagrangian Deployment (GLAD) experiment (Poje et al. 2014). Thanks to these observations, along with a number of high-resolution numerical simulations, the impact of mesoscale and submesoscale currents on the dispersion and transport of physical and biogeochemical tracers in the GoM has been extensively studied (Liu et al. 2011; Zhong and Bracco 2013; Poje et al. 2014; Bracco et al. 2016; Beron-Vera and LaCasce 2016), especially in the northern GoM where the *Deepwater Horizon* incident occurred. In two recent numerical studies, Luo et al. (2016) and Barkan et al. (2017) investigated the role of river runoff in driving submesoscale turbulence in the northern GoM. For example, Barkan et al. (2017) demonstrated that the Mississippi–Atchafalaya River outflow has a strong effect on the strength of submesoscale variability because it modulates the lateral buoyancy gradients and vertical stratification near the surface. Compared to the northern GoM, much less attention has been paid to submesoscale dynamics in the southern part of the eastern basin, in which the main body of the Loop Current (LC) is situated. Considering that most of the mean KE is concentrated along the intense LC and that the LC is host to a vast number of mesoscale eddies (Hamilton et al. 2016; Liu et al. 2016), it is natural to ask how submesoscale turbulence is generated and how it interacts with the background LC and with mesoscale eddies. These issues are key ingredients in understanding the complete energy cycle of the GoM.

The rest of the paper is organized as follows. In section 2, we provide a brief introduction of the multiscale energetics framework and the model output used in this study. Section 3 characterizes the spatial pattern and temporal variability of the scale interactions, flow instabilities, and energy pathways associated with submesoscale variability in the eastern GoM. The main findings of this study are summarized in section 4.

2. Method and data

a. MITgcm llc4320 simulation

We use output from a submesoscale-permitting (nominal horizontal grid spacing of 1/48°) global-ocean simulation conducted with MITgcm (Marshall et al. 1997). The model uses a latitude–longitude–polar cap (llc) horizontal grid configuration with a polar cap that has 4320 × 4320 grid cells (referred to as llc4320). The vertical discretization comprises 90 levels, with a third of these levels above the 400-m depth, enabling high resolution in the upper ocean. The initial conditions were obtained from the 1/6° global-ocean state estimate generated by the Estimating the Circulation and Climate of the Ocean, Phase II (ECCO2) project (Menemenlis et al. 2008), with model spinup occurring at 1/12°, 1/24°, and, finally, 1/48° nominal horizontal grid spacing. The model is forced by 6-hourly atmospheric fields from the 0.14° ECMWF operational atmospheric analysis starting in 2011 and by hourly tidal forcing. The llc4320 output has been extensively used and evaluated against in situ observations in different regions of the global ocean (Rocha et al. 2016; Savage et al. 2017; Qiu et al. 2018; Su et al. 2018). In this study, we use hourly llc4320 output for the 1-yr period that spans September 2011–October 2012 in order to investigate submesoscale energetics in the eastern GoM.

b. Multiscale window transform

In atmosphere–ocean science, the traditional multiscale energetics formalisms can be classified into two types by decomposition technique, one being the Lorenz type (Lorenz 1955), another the Saltzman type. The former is based on Reynolds decomposition, with ensemble mean or its varieties such as time mean, zonal mean, etc., as the background field. The latter is based on Fourier transform and may be referred to as Saltzman type (Saltsman 1957), which is usually applied with respect to space; a recent application is seen in Scott and Wang (2005). One of the major issues with the Lorenz-type or Saltzman-type formalisms is that localization is lost in at least one dimension of space–time to achieve scale decomposition. For this reason, among others, these formalisms have their own limitations in investigating oceanic processes which are generally nonstationary and/or inhomogeneous. To overcome this difficulty, filters have been widely used in place of the Reynolds decomposition or Fourier transform. Now a fundamental question arises: what is the energy of a filtered field? A common practice in the literature is simply to take the square of the filtered field as the energy (up to some constant factor), which is, unfortunately, conceptually incorrect.

To illustrate, suppose a time series $u(t)$ has a simple Fourier expansion with only two frequencies ω_0 and ω_1

$$u(t) = \underbrace{(a_0 \cos\omega_0 t + b_0 \sin\omega_0 t)}_{u^{\sim 0}(t)} + \underbrace{(a_1 \cos\omega_1 t + b_1 \sin\omega_1 t)}_{u^{\sim 1}(t)} . \quad (1)$$

Here we suppose $\omega_0 \ll \omega_1$ so that the low- and high-frequency components [denoted as $u^{\sim 0}(t)$ and $u^{\sim 1}(t)$, respectively] can be easily reconstructed with filters. For this simple example, we know that the energies for the two components are $a_0^2 + b_0^2$ and $a_1^2 + b_1^2$, respectively (i.e., the square of the respective transform coefficients). They are absolutely not equal to the square of the respective reconstructed (filtered) fields, i.e., $[u^{\sim 0}(t)]^2$ and $[u^{\sim 1}(t)]^2$. That is to say, multiscale energy is a concept with the transform coefficients defined in phase space (independent of t here), while $[u^{\sim 0}(t)]^2$ and $[u^{\sim 1}(t)]^2$ are quantities in physical space (functions of t)! These two concepts are related through the well-known Parseval's identity. Particularly, when $u^{\sim 0}(t)$ is a constant (i.e., time mean), we can obtain

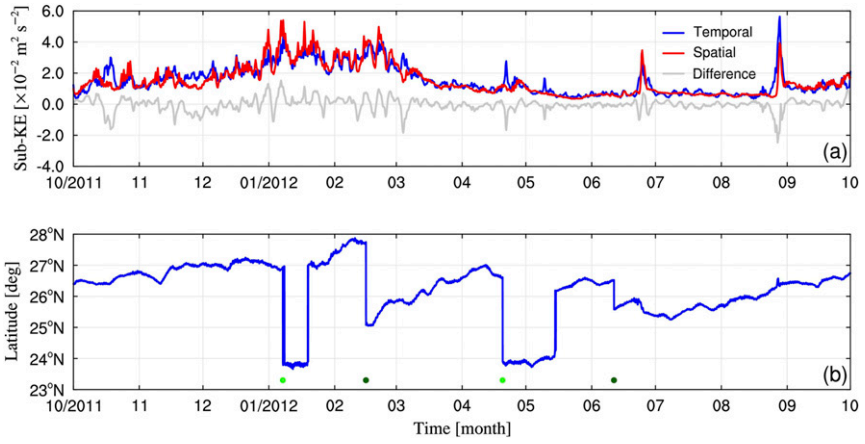

FIG. 1. (a) Time series of the surface KE (10^{-2} m^2 s^{-2}) on the submesoscale window averaged over the eastern GoM (21°–30°N, 90°–82.5°W) based on MWT with cutoff period of 10 days (blue line) and spatial filtering with cutoff scale of 50 km (red line). The gray line indicates the difference between the two time series. A low-pass temporal filter with a cutoff period of 30 h is first applied for both approaches in order to remove the unbalanced internal waves. (b) Time series of the northernmost latitude of the LC axis (defined as the 17-cm SSH contour). The steric part of the SSH (i.e., the area mean of the SSH over the domain) is removed before the calculation. The light green dots indicate the time of the first eddy detachments in the model, with the dark green ones marking the final detachments.

$a_1^2 + b_1^2 = \overline{[u^{\sim 1}(t)]}^2$ (the overbar denotes the time-averaging operator). This explains why the time-averaging operator in the classical energetics formalism cannot be simply removed.

So it is actually a fundamental problem to obtain a *time-dependent* multiscale energy (in this study we perform the scale decomposition in the time domain; similar problem exists when the decomposition is with respect to the space) and has been overlooked in atmosphere–ocean science for decades. The general filters are not suitable because they only yield reconstructions (i.e., filtered variables), with no transform coefficients. Liang and Anderson (2007) developed MWT for this very purpose. They found that, for a class of specially devised orthogonal filters, there exists a transform–reconstruction pair, which is the MWT and its counterpart, multiscale window reconstruction (MWR). In other words, for each MWR $u^{\sim \varpi}(t)$, there is a corresponding transform coefficient $\hat{u}_n^{\sim \varpi}$ (n denotes the discrete time step in the sampling space). The multiscale energy on window ϖ proves to be $(\hat{u}_n^{\sim \varpi})^2$ (cf. Liang and Anderson 2007). It should be noted that orthogonality is essential in defining multiscale energy, otherwise the Parseval's identity does not hold and hence the obtained energy is not the physically consistent energy of the filtered field (Liang and Anderson 2007). As a note, Kang and Curchitser (2017) discussed this issue and found that nonorthogonal filters would lead to inaccurate estimation of the seasonal variability of the kinetic energies of the mean and eddy fields.

To quantify the energy transfers between the background LC, the mesoscale eddies, and the submesoscales that can be resolved by the llc4320 simulation, we perform a three-scale window decomposition of the energy cycle, which is fulfilled by MWT. MWT works to decompose a function space into a direct sum of orthogonal subspaces [termed "scale windows" or simply "windows" by Liang and Anderson (2007)], while preserving the local information (temporal information in this study). Given a time series $u = u(t)$ and considering a three scale window decomposition, $u(t)$ can be reconstructed onto the three windows:

$$u(t) = u^{\sim 0}(t) + u^{\sim 1}(t) + u^{\sim 2}(t), \tag{2}$$

where the $u^{\sim 0}(t)$, $u^{\sim 1}(t)$, and $u^{\sim 2}(t)$ stand for the reconstructions (i.e., filtered series) on the background flow window, the mesoscale window, and the submesoscale window, respectively.

In this study, the submesoscale window is defined to be processes with periods shorter than 10 days and longer than 30 h. The short-period bound for the submesoscale window (i.e., 30 h) is chosen to filter out most of the unbalanced inertia–gravity waves, including internal tides, that are not related to submesoscale turbulence according to previous studies (Rocha et al. 2016; Su et al. 2018). Any balanced submesoscale motions with periods shorter than 30 h are therefore not included in our analysis. The choice of 10 days as the long-period bound for submesoscale variability is consistent with typical time scales of 10–50-km submesoscale processes (Callies et al. 2020), ~10-km wavelengths being the effective resolution of the llc4320 simulation at midlatitudes (Su et al. 2018). One advantage of implementing scale decomposition in the frequency domain is that the resulting energetics retain spatial dependence, which would be lost in traditional, wavenumber-space spectral energetics. In addition, thanks to the localized nature of MWT, the temporal locality is also retained. That is to say, all terms in the energy equations are local in both space and time, allowing for a diagnosis of the energetics at any geographical location and any instant in time. Figure 1 shows a comparison of the

time series of the area-mean submesoscale KE calculated with MWT (blue line) and the traditional approach using a spatial high-pass filter whose cutoff scale is 50 km (red line). The two time series are highly correlated (correlation coefficient of 0.91) with a prevalent seasonal cycle, suggesting that the temporal approach used here is able to separate the submesoscale variations from larger-scale processes, consistent with previous studies (Wang et al. 2018; Zhang et al. 2020).

The mesoscale eddy window is chosen to be bounded by cutoff periods of 180 and 10 days, in accordance with previous studies (Donohue et al. 2016; Yang et al. 2020). Processes with periods longer than 180 days are defined as the background flow, which includes the wax and wane cycle of the LC (Yang et al. 2020). For easy reference, we use notations $\varpi = 0, 1, 2$ to indicate the background flow, mesoscale, and submesoscale windows, respectively.

c. Canonical transfer

Canonical transfer is a key process in the multiscale interactions in fluid flows (e.g., turbulence); it is a faithful quantification of the energy transferred across different scale windows, related to the fundamental processes in geophysical fluid dynamics such as barotropic and baroclinic instabilities (Lorenz 1955; Harrison and Robinson 1978). Canonical transfer was first introduced by Liang and Robinson (2005) (termed "perfect transfer" then), and its form was later rigorously established by Liang (2016). As an illustration, consider a scalar field T in an incompressible flow $\mathbf{u}$:

$$\frac{\partial T}{\partial t} + \nabla \cdot (\mathbf{u}T) = 0. \tag{3}$$

Diffusion is neglected for simplicity. The nonlinear term allows for the interactions between different scales. Taking MWT on both sides of Eq. (3) and multiplying $\hat{T}_n^{\varpi}$ leads to the energy equation on window ϖ:

$$\frac{\partial}{\partial t}\left[\frac{1}{2}(\hat{T}_n^{\varpi})^2\right] = -\hat{T}_n^{\varpi}\nabla \cdot (\widehat{\mathbf{u}T})_n^{\varpi}. \tag{4}$$

An intriguing and difficult problem is to separate the term on the right-hand side of Eq. (4) to obtain a "transfer" term that represents energy exchanges across different scales and a "transport" term that redistributes energy in physical space (i.e., a divergence term). It has long been recognized that the separation is not unique (e.g., Holopainen 1978; Plumb 1983), which makes the *local* interpretation of the energy transfer between scales quite ambiguous (the *global* integration of all those transfer formalisms appeared in literature is the same). By reconstructing the "atomic" energy fluxes on the multiple scale windows using MWT, Liang (2016) found that this problem solvable and proved that a natural and unique transfer expression follows:

$$\Gamma_n^{\varpi} = \frac{1}{2}\left[(\widehat{\mathbf{u}T})_n^{\varpi} \cdot \nabla \hat{T}_n^{\varpi} - \hat{T}_n^{\varpi}\nabla \cdot (\widehat{\mathbf{u}T})_n^{\varpi}\right]. \tag{5}$$

Readers are referred to Liang (2016, section 3) for a rigorous derivation. Equation (4) bears a Lie bracket form, reminiscent of the Poisson bracket in Hamiltonian mechanics. Furthermore, it satisfies a very important property:

$$\sum_{\varpi}\sum_{n} \Gamma_n^{\varpi} = 0, \tag{6}$$

as proved in Liang (2016), which means that canonical transfers are interscale processes that preserve energy. This seemingly obvious fact, however, does not hold in other traditional formalisms. To distinguish, Liang (2016) termed Eq. (4) the "canonical transfer." Previously, Liang and Robinson (2007) showed that, for a benchmark barotropic model whose instability structure is analytically known, the traditional formalism fails to give the correct source of instability, while canonical transfer does.

It is worth noting that a recent work by Aluie et al. (2018) also noticed the "transfer-transport separation" problem. In their study, Aluie et al. (2018) tried to define the energy transfer [localized in space, see Eq. (7) in their study] by satisfying the Galilean invariance criterion, which requires that the energy transfer at an arbitrary location should be independent of the velocity of the observer. They did not mention whether their expression preserved the energy across spatial scales. Also note that their energetics formalism is established with a spatial filter (i.e., coarse-graining approach) in place of Fourier transform, in order to achieve the localization of the energetics. However, the energy is defined by the square of the filtered field in their study, which is not the case by concept (see the multiscale energy representation issue in section 2b).

d. Localized multiscale energy equations

Using MWT, the kinetic energy (KE) and available potential energy (APE) equations on scale window ϖ can be derived from the primitive equations:

$$\frac{\partial K^{\varpi}}{\partial t} = \Gamma_K^{\varpi} + b^{\varpi} + \Delta Q_K^{\varpi} + \Delta Q_P^{\varpi} + F_K^{\varpi}, \quad \text{and} \tag{7}$$

$$\frac{\partial A^{\varpi}}{\partial t} = \Gamma_A^{\varpi} - b^{\varpi} + \Delta Q_A^{\varpi} + S_A^{\varpi} + F_A^{\varpi}. \tag{8}$$

The expressions and meanings for the above symbols are listed in Table 1. Readers are referred to Liang (2016) for a detailed derivation. Equations (7) and (8) have been utilized to diagnose the diverse dynamical processes in atmospheric and oceanic motions such as Monterey Bay processes (Liang and Robinson 2009), LC eddy shedding (Yang et al. 2020), storm track dynamics (Zhao and Liang 2018), sudden stratospheric warming (Xu and Liang 2017), and atmospheric blocking (Ma and Liang 2017), to name a few. Note that the definition of APE used here is under the quasigeostrophic (QG) approximation (see Table 1), which assumes that the density perturbation is small compared with the reference stratification. The limitation of this definition will be discussed later, in section 4.

The canonical transfers, i.e., the Γ terms in Eqs. (7) and (8), are still in a cumulated form and need to be further decomposed in order to select out the components between two designated windows in a three-scale window framework.

TABLE 1. Mathematical form and meaning of the energy terms in Eqs. (7) and (8). The variable notations are conventional. For details, see Liang (2016).

Symbol	Mathematical form	Meaning
K^{ϖ}	$\frac{1}{2}\hat{\mathbf{v}}_h^{\sim\varpi}\cdot\hat{\mathbf{v}}_h^{\sim\varpi}$	KE on window ϖ
ΔQ_K^{ϖ}	$-\frac{1}{2}\nabla\cdot\left[\widehat{(\mathbf{v}\mathbf{v}_h)}^{\sim\varpi}\cdot\hat{\mathbf{v}}_h^{\sim\varpi}\right]$	KE transport on window ϖ
Γ_K^{ϖ}	$\frac{1}{2}\left[\widehat{(\mathbf{v}\mathbf{v}_h)}^{\sim\varpi}:\nabla\hat{\mathbf{v}}_h^{\sim\varpi}-\nabla\cdot\widehat{(\mathbf{v}\mathbf{v}_h)}^{\sim\varpi}\cdot\hat{\mathbf{v}}_h^{\sim\varpi}\right]$	Canonical KE transfer to window ϖ
ΔQ_P^{ϖ}	$-\frac{1}{\rho_0}\nabla\cdot(\hat{\mathbf{v}}^{\sim\varpi}\hat{P}^{\sim\varpi})$	Pressure work on window ϖ
b^{ϖ}	$-\frac{g}{\rho_0}\hat{\rho}^{\sim\varpi}\hat{w}^{\sim\varpi}$	Buoyancy conversion on window ϖ. Positive b^{ϖ} means a conversion from APE to KE on window ϖ.
A^{ϖ}	$\frac{1}{2}c(\hat{\rho}^{\sim\varpi})^2,\ c=\frac{g^2}{\rho_0^2N^2}$	APE on window ϖ; N is the buoyancy frequency, which is horizontally and temporally avergaed.
ΔQ_A^{ϖ}	$-\frac{1}{2}\nabla\cdot\left[c\hat{\rho}^{\sim\varpi}\widehat{(\mathbf{v}\rho)}^{\sim\varpi}\right]$	APE transport on window ϖ
Γ_A^{ϖ}	$\frac{c}{2}\left[\widehat{(\mathbf{v}\rho)}^{\sim\varpi}\cdot\nabla\hat{\rho}^{\sim\varpi}-\hat{\rho}^{\sim\varpi}\nabla\cdot\widehat{(\mathbf{v}\rho)}^{\sim\varpi}\right]$	Canonical APE transfer to window ϖ
S_A^{ϖ}	$\frac{1}{2}\hat{\rho}^{\sim\varpi}\widehat{(w\rho)}^{\sim\varpi}\frac{\partial c}{\partial z}$	Apparent source/sink of APE that is due to the nonlinearity of the reference stratification on window ϖ
F_K^{ϖ}	Not explicitly expressed but treated as a residue term in the KE budget equation	Change rate of KE due to wind stress and internal dissipation on window ϖ
F_A^{ϖ}	Not explicitly expressed but treated as a residue term in the APE budget equation	Change rate of APE due to buoyancy flux and diffusion on window ϖ

This is done by a procedure called "interaction analysis," explained in detail in Liang and Robinson (2005). Regarding the canonical KE transfer on the submesoscale window ($\varpi = 2$), the interaction analysis gives $\Gamma_K^{0\to2}$ and $\Gamma_K^{1\to2}$, which indicates the transfers of KE to the submesoscale window ($\varpi = 2$) from the background flow window ($\varpi = 0$) and from the mesoscale window ($\varpi = 1$), respectively. A positive $\Gamma_K^{0\to2}$ or $\Gamma_K^{1\to2}$ means a release of, respectively, background or mesoscale flow KE for the growth of submesoscale turbulence, which is indicative of the occurrence of barotropic instability. Similarly, $\Gamma_A^{0\to2}$ and $\Gamma_A^{1\to2}$ are the two scale interaction properties in the APE equation of the submesoscale flow, which represent, respectively, the transfer of APE between the background flow and submesoscale windows and the transfer of APE between the mesoscale and submesoscale windows. A positive $\Gamma_A^{0\to2}$ or $\Gamma_A^{1\to2}$ is indicative of baroclinic instability. In the following, we will focus on the energetics on the submesoscale window ($\varpi = 2$).

The energetics on the mesoscale window that is closely related with the LC eddy shedding phenomenon were recently studied by Yang et al. (2020), using the same methodology as we do here. They found that barotropic instability provides the energy sources for the generation of the mesoscale eddies in the western (upstream) branch of the LC, while baroclinic instability further favors the growth of these eddies that propagate downstream to the northeastern portion of the LC, eventually causing the shedding of the LC anticyclonic eddy. Note that the submesoscale processes are not resolved by the coarse grid simulation used in Yang et al. (2020). The underlying energetics associated with the submesoscales is still unknown. In fact, as will be shown later, the spatial–temporal characteristics of the submesoscale energetics are generally quite different from that of the mesoscales as found in Yang et al. (2020). For instance, the strongest submesoscale KE signal is concentrated in the northeastern GoM which undergoes a significant seasonal cycle, while the strongest mesoscale KE signal is confined in the LC region which is closely related with the eddy shedding process (see Fig. 7 in Yang et al. 2020). This implies distinct generation mechanisms regarding to the processes in these two scales, motivating us to investigate the submesoscale energetics in this paper.

3. Spatiotemporal variations of submesoscale energetics

a. Submesoscale kinetic energy

The time series of the submesoscale KE (K^2) averaged over the eastern Gulf exhibits a strong seasonal cycle with higher values during winter (Fig. 1a). Unlike mesoscale KE, which is highly related with the LC eddy shedding process (Hamilton et al. 2019; Yang et al. 2020), the submesoscale KE does not show a clear correlation with the LC configuration (Fig. 1b). In addition to the seasonal variation, the K^2 time series also displays intermittent peaks at synoptic time scales, which are likely due to short-term atmospheric forcings such as hurricanes or storms passing over the Gulf.

To examine the geographic variability of the submesoscale turbulence, we plot the instantaneous vorticity and K^2 fields on a typical winter day (28 January 2012) and a summer day (25 July 2012) (Figs. 2a–d). An observation is that both fields exhibit larger magnitudes during winter than summer, especially in the northern basin, consistent with previous studies (Luo et al. 2016; Barkan et al. 2017). Another observation is that enhanced values of vorticity and K^2 are concentrated

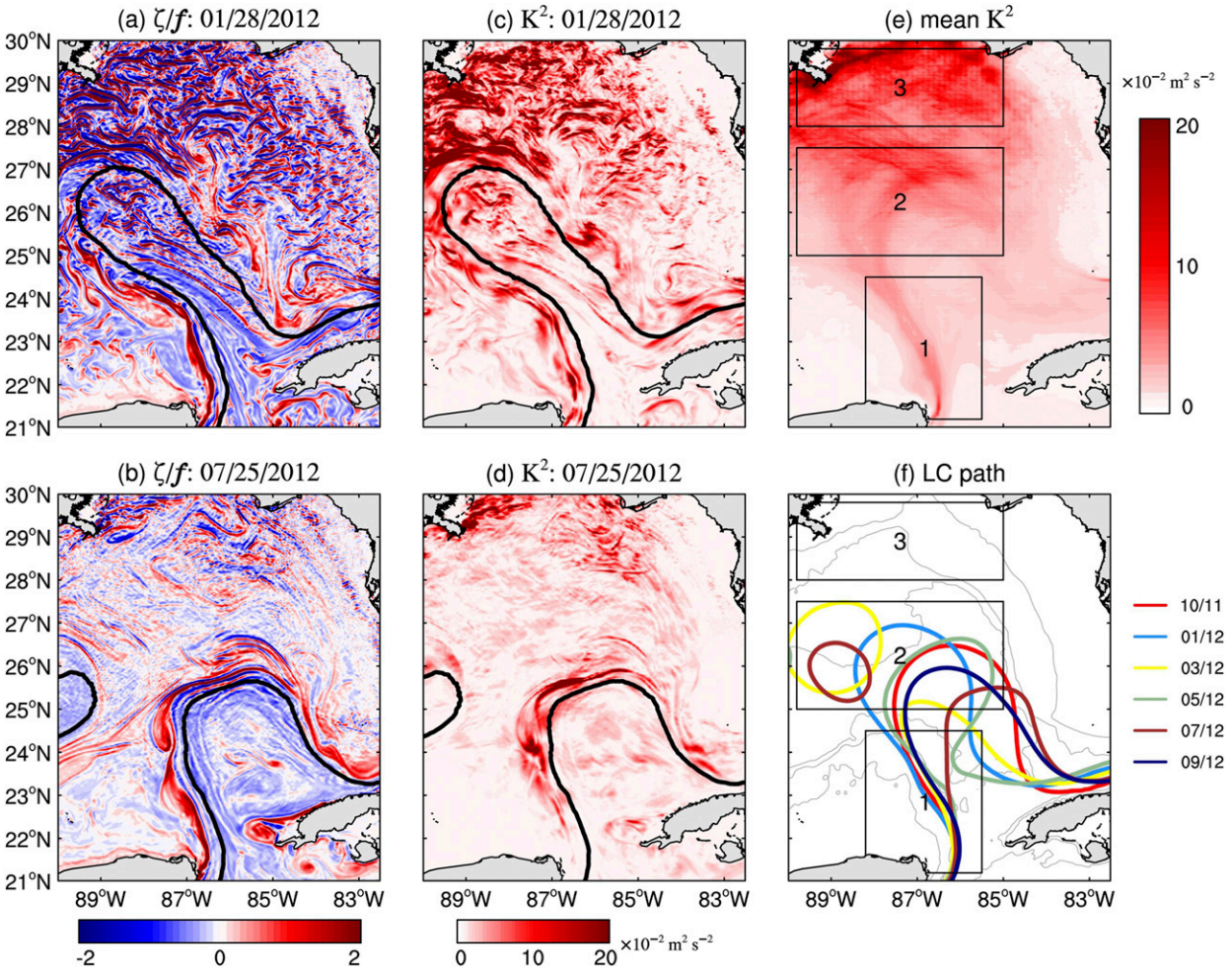

FIG. 2. Snapshots of the normalized relative vorticity ζ/f at the surface: (a) 28 Jan and (b) 25 Jul 2012. The black contour denotes the instantaneous 17-cm SSH contour. (c),(d) As in (a) and (b), but for the surface submesoscale KE (K^2; 10^{-2} m^2 s^{-2}). (e) Map of the annually averaged surface K^2 (10^{-2} m^2 s^{-2}). The three analysis subdomains are marked and labeled in (e): the eastern Campeche Bank shelf (region 1), the deep basin of eastern GoM (region 2), and the northern GoM (region 3). (f) The monthly mean LC axis (color contours; defined by the 17-cm SSH contour) during the period from October 2011 to September 2012. The light gray contours in (f) represent the 100-, 1000-, and 3000-m isobaths.

along the periphery of the LC. These features are associated with frontal eddies that have horizontal scales < 100 km and temporal scales of $O(1)$ days in the deep basin and with across-isobath flow (bottom pressure torque) in the vicinity of the shelf slope (e.g., Weisberg et al. 2001). For the deep basin, they appear to be more active in the western branch of the LC, without a clear seasonality.

In the following, we choose three subdomains, that is, the shelf region along the eastern Campeche Bank, the deep basin of the eastern Gulf and the northern GoM, to study the regional characteristics of the submesoscale energetics in the eastern GoM. These subdomains are marked as 1–3, respectively (Fig. 2e). In region 1, the annual-mean K^2 pattern is characterized by enhanced values concentrated within a narrow strip along the steady LC which flows northward following the topography of the Campeche Bank slope (Figs. 2e,f). In the vertical, the K^2 is largely confined in the mixed layer and decays rapidly with depth (Fig. 3a). Note that the K^2 averaged over this region does not show a significant seasonality. This indicates that the seasonally dependent mixed layer baroclinic instability might be ruled out as the generation mechanism of the submesoscale turbulence in this region. In contrast to region 1, the K^2 averaged over regions 2 and 3 exhibit a significant seasonal cycle with winter/summer maximum/minimum (Figs. 3e,i), similar to those seen in other ocean sectors (Mensa et al. 2013; Callies et al. 2015; Rocha et al. 2016). A major difference between these two regions is that the region 2 is influenced by the large-scale background LC and its detached anticyclonic eddies, while the region 3 is absent from the direct impact of LC during the entire simulation period (Fig. 2f). Another noticeable difference is that, during summer, large magnitude of K^2 is seen along the shelf region (i.e., shallower than 100 m) of the northern GoM

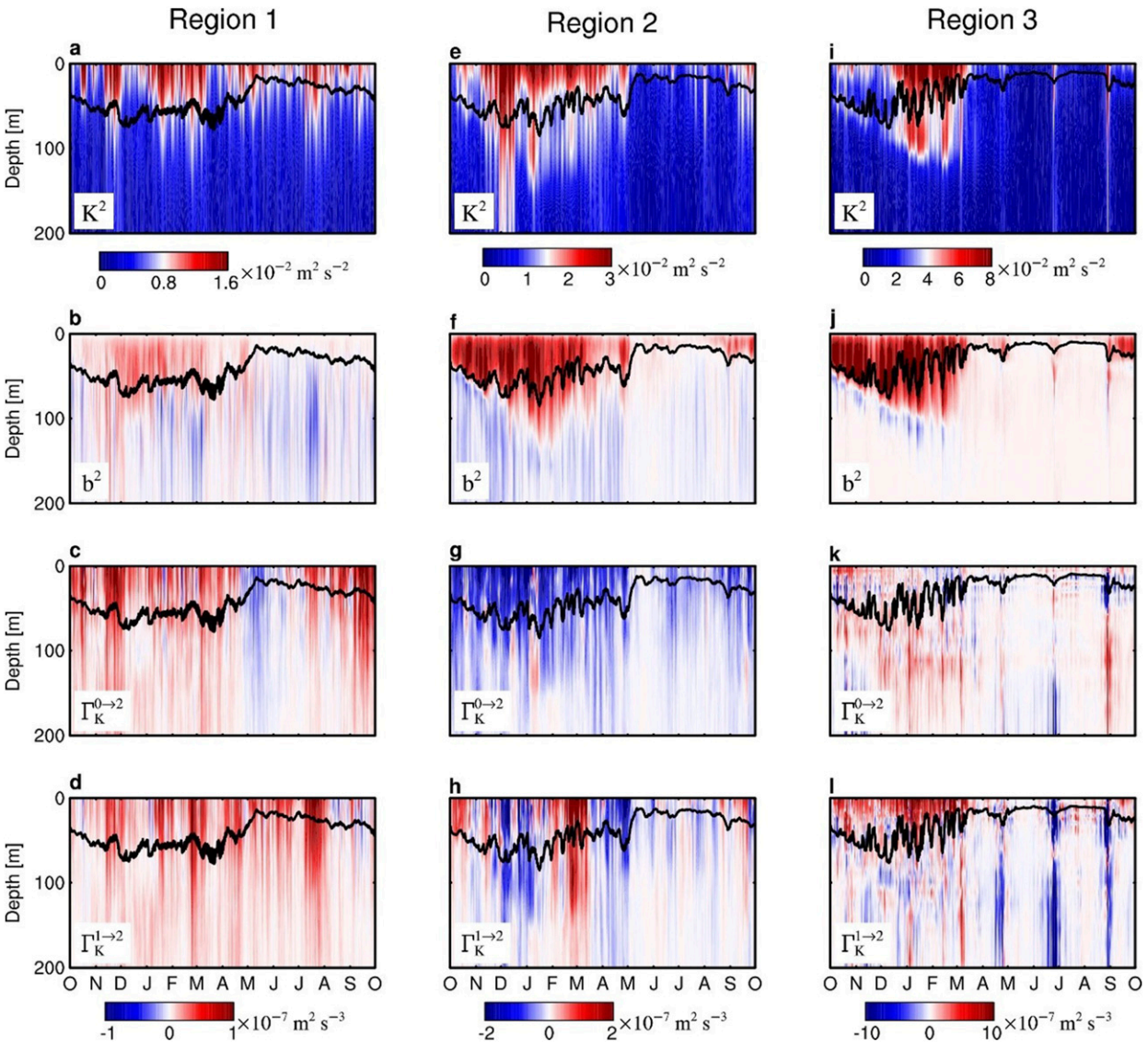

FIG. 3. Depth–time diagram of the spatially averaged (a),(e),(i) K^2 ($10^{-2}\,m^2\,s^{-2}$); (b),(f),(j) b^2 ($10^{-7}\,m^2\,s^{-3}$); (c),(g),(k) $\Gamma_K^{0\to2}$ ($10^{-7}\,m^2\,s^{-3}$); and (d),(h),(l) $\Gamma_K^{1\to2}$ ($10^{-7}\,m^2\,s^{-3}$) for the three regions delineated in Fig. 2e. The black line in each figure denotes the spatially averaged MLD. The MLD is defined as the depth at which the temperature is 0.2°C below that at the surface (de Boyer Montégut et al. 2004).

(region 3), meanwhile the intensity of K^2 over the deep basin (region 2) is substantially weak (Fig. 2d), consistent with Barkan et al.'s (2017) modeling results. As will be seen below, the energy pathways among the three subdomains are quite different, suggesting that the generation and dissipation mechanisms of the submesoscale turbulence are geographically inhomogeneous.

b. Buoyancy conversion

The rate of buoyancy conversion b^2 measures the converting process between A^2 and K^2 reservoirs. Positive b^2 represents a conversion of submesoscale APE to KE and is usually associated with submesoscale generation (Fox-Kemper et al. 2008; McWilliams 2016). The generation mechanism of the submesoscales can be attributed to various processes, such as mixed layer baroclinic instabilities and strain-induced frontogenesis. Both processes have been shown to have positive b^2 near the surface (McWilliams 2016). Figure 4a shows the horizontal distribution of vertically integrated (upper 100 m) b^2 averaged over the 1-yr simulation period (top panel), the winter months [December–February (DJF); middle panel] and the summer months [June–August (JJA); bottom panel]. The b^2 is dominantly positive and large values are mainly distributed in the northern basin, indicating a strong submesoscale generation in this area. Not surprisingly, the magnitude of b^2 in the northern basin is noticeably larger in

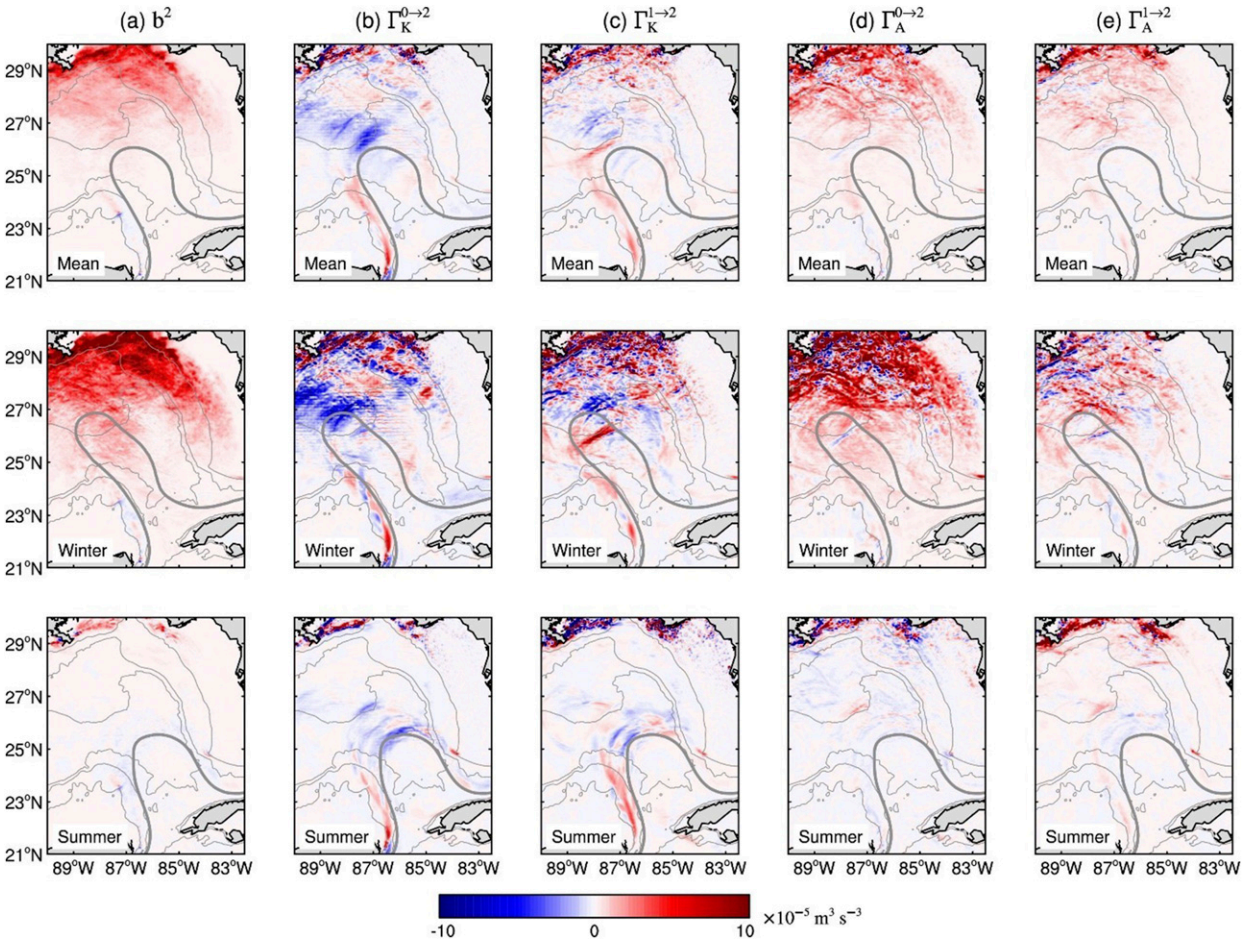

FIG. 4. Horizontal maps of depth-integrated (upper 100-m depth) energetics (color shading; 10^{-5} m^3 s^{-3}) averaged over (top) the whole simulation period (1 year), (middle) the winter months (DJF), and (bottom) the summer months (JJA), showing (a) b^2, (b) $\Gamma_K^{0\to2}$, (c) $\Gamma_K^{1\to2}$, (d) $\Gamma_A^{0\to2}$, and (e) $\Gamma_A^{1\to2}$. The 17-cm SSH contour averaged in each time period is superimposed (in thick gray).

winter than summer, in agreement with the seasonality of K^2 (Figs. 2c,d).

To further explore the roles of mixed layer instability and frontogenesis in the submesoscale generation, we compare the time series of b^2 (colored contours in the second panel of Fig. 3), with that of the mixed layer depth (MLD; see the black lines in the second panel of Fig. 3) and the frontogenesis function (Fig. 5) for the three considered subdomains. From the equation of density gradient, the frontogenesis tendency consists of straining deformations by horizonal velocity and vertical velocity, and processes associated with horizontal diffusion and vertical mixing [see Capet et al. (2008c) and Barkan et al. (2019) for details]. The horizontal straining effect is typically considered as the dominant process for frontogenesis. The vertical straining effect usually acts to weaken the lateral density gradient due to an ageostrophic circulation in response to the sharpening of the density gradient generated by the horizontal counterpart (Capet et al. 2008c; Gula et al. 2014). The diffusion and mixing processes are generally frontolytic. Therefore, in this study, the frontogenesis function is defined as the straining deformation by the horizonal velocity, i.e.,

$$F_s = \mathbf{Q}_s \cdot \nabla_h \rho_\theta, \tag{9}$$

where

$$\mathbf{Q}_s = -(\partial_x u \partial_x \rho_\theta + \partial_x v \partial_y \rho_\theta, \partial_y u \partial_x \rho_\theta + \partial_y v \partial_y \rho_\theta), \tag{10}$$

and ρ_θ is the potential density. This definition has been widely used in literature (e.g., Hoskins 1982; Siegelman 2020)

Region 3 has the strongest buoyancy conversion among the three subdomains and displays a clear winter maximum which corresponds to the seasonal phase of the MLD and F_s (Figs. 3j and 5c). This suggests that both mixed layer instability and strain-induced frontogenesis are at work in this region. It is interesting to note that intense frontolysis occurs beneath the mixed layer, especially during September–November. This particular feature is not observed in the other two regions; we leave its underlying mechanism to future studies. In region 2, K^2, b^2, MLD, and F_s roughly share the same seasonal cycle with a clear winter maximum, indicating that both the

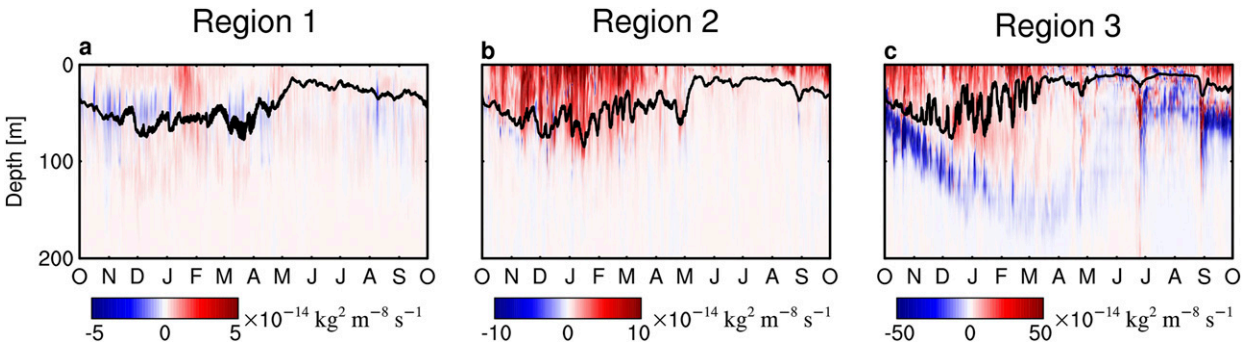

FIG. 5. As in Fig. 3, but for the frontogenesis function F_s (10^{-14} kg^2 m^{-8} s^{-1}) for the three regions. For easy comparison, the ratio of the color scales among the three plots are chosen as the same as the bottom panels of Fig. 3.

mixed layer instability and frontogenesis are responsible for the submesoscale generation in this area (Figs. 3e,f and 5b). An in-depth evaluation of the energization of the submesoscales in this region through these two mechanisms is beyond the scope of this study. Region 1 has a relatively small b^2 and F_s; besides, no significant correlation is found between b^2 and K^2 (recall that the K^2 in this region does not have a clear seasonality), and between F_s and b^2 (Figs. 3a,b and 5a). This implies that neither the mixed layer instability nor frontogenesis is the primary factor determining the submesoscale production in this region.

c. *Canonical transfers of KE and APE*

As introduced in section 2, the energy transfers across different temporal scales is quantified by the canonical transfers in a localized (both in space and time) format. We first examine the canonical transfers of KE to the submesoscale window from the background flow and mesoscale windows which are indicated by calculation $\Gamma_K^{0\to2}$ and $\Gamma_K^{1\to2}$, respectively. Figures 4b and 4c respectively show the horizontal distribution of vertically integrated (upper 100 m) $\Gamma_K^{0\to2}$ and $\Gamma_K^{1\to2}$ averaged over the 1-yr simulation period (top panel), winter (middle panel), and summer (bottom panel). Both terms exhibit large and positive values on the western side of the LC. This indicates that the LC along the Campeche Bank slope is barotropically unstable, resulting in strong downscale KE transfers to the submesoscale processes. The time series of both terms averaged in this subdomain (region 1) exhibit irregular variabilities throughout the simulation period, which could explain the absence of a clear submesoscale seasonal cycle observed in this region (Figs. 3a,c,d). In addition, the small magnitude of b^2 (Fig. 3b) further confirms that the production of K^2 is mainly due to barotropic instability. By using the same procedure, Yang et al. (2020) found that the mesoscale perturbations in this region are mainly generated by the strong forward KE transfer from the background LC to the mesoscale eddies (similar result can be obtained by calculating $\Gamma_K^{0\to1}$ here; not shown). These results indicate that barotropic instability is the dominant mechanism to generate perturbations (both mesoscale and submesoscale) in this region. Similar scenario is also found in other topographically regions such as the Bismarck Sea (Srinivasan et al. 2017) and the Gulf Stream (Gula et al. 2016) in realistic regional models.

In contrast to the forward KE routes along the shelf slop of the Campeche Bank, a strong negative pool of $\Gamma_K^{0\to2}$ is observed in the deep basin (Fig. 4b). This feature indicates that the submesoscale turbulence is losing KE to the background flow via inverse cascade of KE. The negative $\Gamma_K^{0\to2}$ pool is much pronounced in winter during which the LC extends well into the deep basin, while it remains in a weak magnitude and a southward position (due to the retraction of the LC) during the summer (Figs. 3g and 4b). Inverse KE cascade from the submesoscale window to the mesoscale window (i.e., negative $\Gamma_K^{1\to2}$) is also seen in this region (Figs. 3h and 4c), although with a smaller spatial coverage and a weaker amplitude compared to $\Gamma_K^{0\to2}$. Further north, the canonical KE transfers display a rather noisy spatial pattern with positive and negative values mingled with each other. From an area-average perspective, $\Gamma_K^{1\to2}$ has a larger amplitude than $\Gamma_K^{0\to2}$ and positively peaks in winter in this region (region 3; Figs. 3k,l). This indicates that the forward KE cascade from the mesoscale flows serves as a KE source for the wintertime submesoscale turbulence in the near surface of this region, although its contribution is secondary compared to the dominant buoyancy production (i.e., positive b^2; see Figs. 3j and 4a). It is interesting to note that strong inverse KE cascade episodically occurs in the subsurface layers (below 100 m) of this region, especially during the summer and fall seasons (Fig. 3l). These deep-reaching inverse cascade processes, which are likely the aftermath of the injection of strong KE by high-frequency wind forcing during the passages of Tropical Storm Debby (June 2012) and Hurricane Isaac (August 2012), serve as a source term in the local mesoscale KE budget.

The above results suggest that the KE transfers between the submesoscale and larger-scale processes (i.e., background flow and mesoscale eddies) are highly inhomogeneous in space. Particularly, we found a coherent pool of inverse KE cascade from the submesoscale window to the background flow window in the north flank of the LC. Two factors seem to be essential for the formation of this coherent inverse cascade center: a sufficient reservoir of submesoscale KE and an existence of a strong background current. The first factor implies that the inverse cascade process would occur preferentially in the

northern GoM and in winter where and when the submesoscale turbulence is most active. The second factor explains why significant inverse cascade only appears in region 2 where the LC frequently extends and retracts, instead of region 3 in which the submesoscale turbulence is not directly influenced by the LC during the simulation period. Similar upscale KE transfer routes are also found in other ocean sectors with strong currents, such as the Kuroshio Extension (Sasaki et al. 2014). Our results seem to be consistent with Brüggemann and Eden (2015) who found that forward route to dissipation is less efficient when the flow is in quasigeostrophic balances (like the region 2 case) than in ageostrophic conditions (like the region 3 case), using a set of numerical model configurations of a baroclinically unstable flow system.

The cross-scale transfers of APE to the submesoscale window from the background flow and mesoscale windows are quantified by $\Gamma_A^{0\to2}$ and $\Gamma_A^{1\to2}$, respectively. The horizontal distributions of the two terms are shown in Figs. 4d and 4e for the mean (top), winter (middle), and summer (bottom). Both terms feature strong and dominantly positive values in the north basin, indicating that the APE cascades are mainly forward, consistent with previous studies (Capet et al. 2008a; Molemaker and McWilliams 2010). During the winter months, the APE transferred to the submesoscales is mainly from the large-scale background flow (i.e., $\Gamma_A^{0\to2}$), and is further converted to KE via buoyancy conversion, consistent with the typical energy pathway of baroclinic instability (e.g., Pedlosky 1987; von Storch et al. 2012). During the summer months, $\Gamma_A^{1\to2}$ plays the leading role with localized positive values confined along the coastal areas of the northern GoM (bottom panel of Fig. 4e). Meanwhile, the buoyancy conversion is merely in a moderate strength in this region (bottom panel of Fig. 4c). This is in agreement with a strong summer riverine frontogenesis in the northern GoM as reported in Luo et al.'s (2016) numerical study. Finally, we emphasize that canonical transfers and buoyancy conversion form only a part of the energy budget. Some energy reservoirs in Fig. 4 exhibit unbalanced sources or sinks, which must be balanced by other processes such as nonlocal transports, pressure work, work done by wind stress and buoyancy forcing, or internal dissipations. In the next subsection, we perform an energy budget analysis to seek out more information about the submesoscale energetics in the respective regions.

d. Energy budget

Figure 6 shows the volume-averaged submesoscale KE (K^2; top row) and APE (A^2; bottom row) budgets for the three subdomains. Each budget term is vertically averaged in the upper 100-m water column, and temporally averaged over the 1-yr simulation period (green bar), the winter months (blue bar), and the summer months (red bar). To see how energy is redistributed in the vertical, we split the ΔQ_P^2 term into its horizontal component ($\Delta_h Q_P^2$) and vertical component ($\Delta_z Q_P^2$). The vertical components of the other two nonlocal terms (i.e., ΔQ_K^2, and ΔQ_A^2) are negligible compared to their horizontal counterparts, and hence are not explicitly shown here. In region 1, along the shelf slope of eastern Campeche Bank, the K^2 balance is dominated by $\Gamma_K^{0\to2}$, $\Gamma_K^{1\to2}$, ΔQ_K^2, $\Delta_z Q_P^2$, and F_K^2 (Fig. 6a). Note that the residue term F_K^2 includes external forcing and internal dissipation which are not separately diagnosed since certain variables are not available from the model outputs. Nevertheless, one can infer that forcing (possibly wind forcing since we are considering the top 100 m) or dissipation is the dominant process when F_K^2 is positive or negative, respectively. The forward KE cascades from the background flow and mesoscale eddies (positive $\Gamma_K^{0\to2}$ and $\Gamma_K^{1\to2}$) serve as the main sources of submesoscale KE in this region and they are balanced by outgoing energy advection (negative ΔQ_K^2), downward transport by vertical pressure work (negative $\Delta_z Q_P^2$) and dissipation processes (negative F_K^2). These energetic processes do not exhibit a significant seasonality except for the dissipation term which is about 3 times larger in magnitude during winter than summer. Compared to the K^2 budget, the A^2 budget terms averaged in this region are generally in small magnitude (Fig. 6b), indicating that barotropic processes are the dominant mechanisms in generating the submesoscale turbulence along the shelf of the Campeche Bank.

Regarding the energy pathway in the deep basin (region 2), the major source for the winter K^2 is from buoyancy production (i.e., positive b^2), which is mainly balanced by inverse KE cascade from the submesoscale turbulence to the background flow (i.e., negative $\Gamma_K^{0\to2}$) (Fig. 6c). This seems to be consistent with the energy routes in the context of a surface-intensified Charney-like baroclinic instability, which is characterized by a significant input of KE in the mesoscale and submesoscale ranges by extraction of energy from the APE reservoir and an overwhelming inverse cascade of KE (Sasaki et al. 2014; Capet et al. 2016). During the summer, the b^2 is negligible due to shallow mixed layer and weak frontogenesis processes. Instead, the submesoscale KE is generated by external forcings (i.e., positive F_K^2) and is balanced by inverse KE cascade from the submesoscales to the background flow (i.e., negative $\Gamma_K^{0\to2}$), although with a smaller amplitude relative to the winter case. As for the winter A^2 budget in this region, the submesoscale APE reservoir is mainly fueled by $\Gamma_A^{0\to2}$ and to a lesser extent from $\Gamma_A^{1\to2}$, and is balanced by the buoyancy conversion to KE and another term S_A^2 (Fig. 6d). As explained in Table 1, S_A^2 is an apparent source/sink due to the nonlinearity of the reference stratification. Mathematically, this additional term comes from the separation of transfer and transport processes in the multiscale APE equation due to a stratified profile $c = c(z)$ (cf. Liang 2016). For a linear reference stratification (i.e., c = constant), this term becomes zero. Generally, this term can be neglected in the ocean interior ($\partial c/\partial z$ is very small). But it could be large in the surface mixed layer ($\partial c/\partial z \neq 0$), especially during winter when large fluctuations of vertical velocity and density occur. It can be seen from Fig. 6d that S_A^2 acts as a major sink of A^2 during the winter season.

The northern GoM (region 3) contains the strongest submesoscale signal in the GoM; the intensities of the submesoscale energetics averaged over this subdomain are in general one order of magnitude larger than those in the other two subdomains (Figs. 6e,f). During winter, the dominant source of K^2 is from b^2 through mixed layer baroclinic instability and is

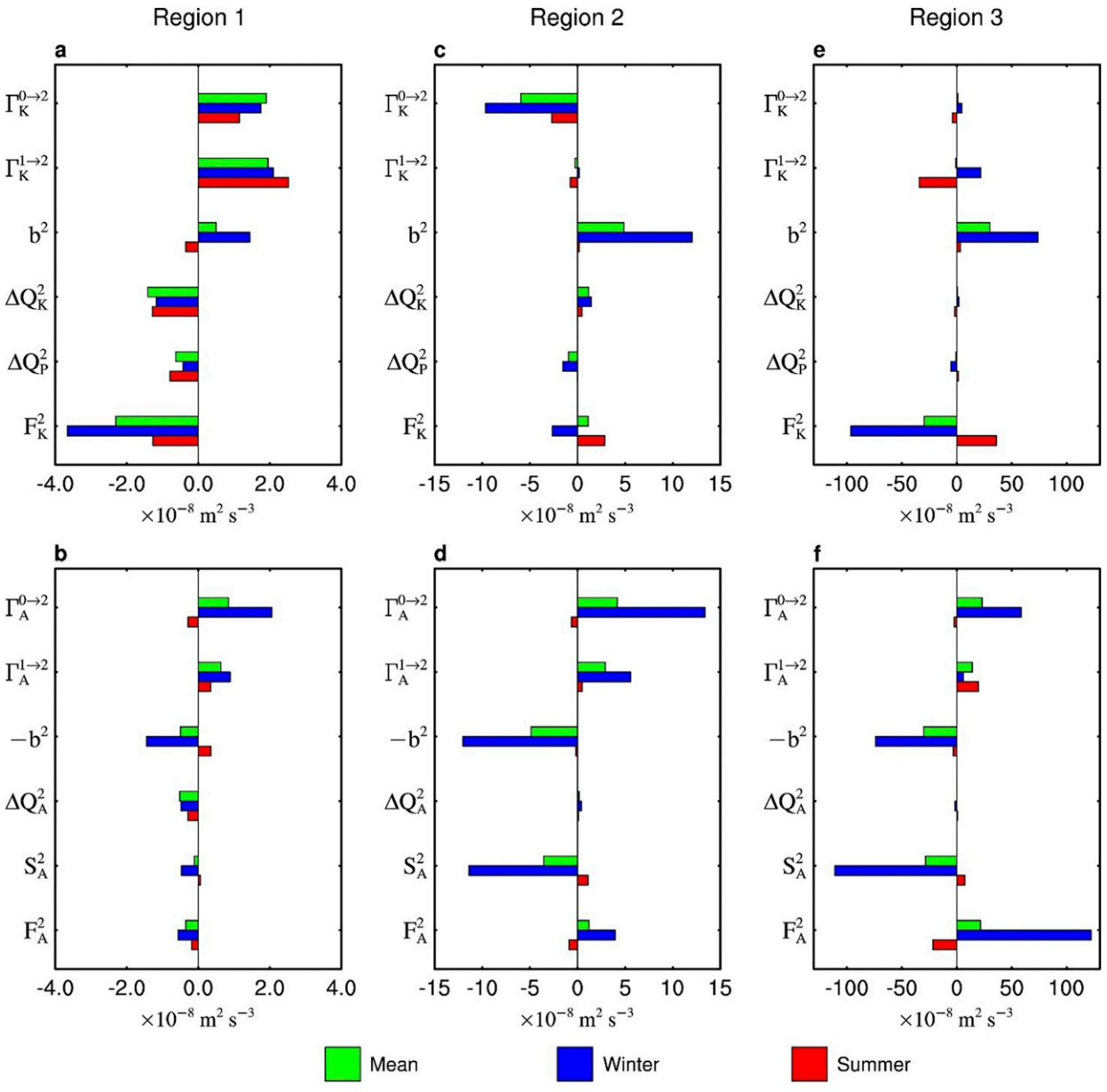

FIG. 6. The (a),(c),(e) KE and (b),(d),(f) APE budgets averaged over the three subdomains defined in Fig. 2e. The volume averaging is taken over the upper 100-m water column. The energy terms are all in units of $10^{-8}\,m^2\,s^{-3}$. The green, blue, and red bars indicate budget terms averaged over the 1-yr simulation period, the winter months (DJF), and the summer months (JJA), respectively.

balanced by strong dissipation (negative F_K^2). This is different from the energy route as we found in region 2 where the regional K^2 is mostly depleted by inverse KE cascades. As discussed earlier, a possible reason for the distinctive features between these two regions is that the direction of the KE transfer in the submesoscale range may have a strong dependence on the dynamical conditions of the background flow (Brüggemann and Eden 2015). In contrast, the summer K^2 balance is overall between the positive F_K^2 and negative $\Gamma_K^{1\to2}$, manifesting the episodical strong wind events that energize the upper submesoscale currents followed by an inverse cascade of KE to the mesoscale flows (see also Fig. 3l). From the A^2 budget, we can see that surface buoyancy forcing (i.e., positive F_A^2) serves as the dominant source for the winter submesoscale APE reservoir and the S_A^2 represents a strong sink of APE in the upper ocean. The net contribution of the two processes to the APE changes is small. The overall balance between the forward APE cascade (i.e., $\Gamma_A^{0\to2}>0$) and APE to KE conversion (i.e., $b^2>0$) during the winter months indicates a dominant baroclinic instability mechanism. In summer, the regional A^2 balance is controlled by $\Gamma_A^{1\to2}$ and F_A^2. The positive $\Gamma_A^{1\to2}$, which is concentrated along the coastal regions (see the bottom panel of Fig. 4e), indicates a

mesoscale strain-induced frontogenesis by river outflows at the surface of this region (Luo et al. 2016; Barkan et al. 2017). Finally, we note that nonlocal processes (i.e., ΔQ_K^2 and ΔQ_P^2) are generally negligible in the energy balance of the submesoscales in regions 2 and 3 (Figs. 6c–f), suggesting that the submesoscale dynamics are dominated by local processes in these two subdomains.

4. Summary and discussion

In this study, a localized multiscale energetics diagnostic methodology is employed to investigate the spatiotemporal variations of submesoscale energetics in the eastern GoM, using output from the 1/48° MITgcm llc4320 simulation. The diagnostic budget equations are based on a three-scale window decomposition, with which the related fields are decomposed into a background flow window, a mesoscale window, and a submesoscale window in the frequency domain. The resulting KE and APE energetics are localized in both time and space domains, allowing us to examine the spatial structure and temporal variability of the underlying energetics of the submesoscale currents.

By diagnosing the canonical transfer between the background flow and the submesoscale windows and that between the mesoscale and the submesoscale windows, we found that the energy cascades associated with the submesoscales are geographically highly inhomogeneous in the GoM:

- Along the shelf region of the eastern Campeche Bank, barotropic instability is the dominant mechanism in generating the submesoscale eddies. Strong positive KE transfers to the submesoscales from the background flow as well as mesoscale eddies are seen, while the APE transfers and buoyancy conversion are not significant and thus baroclinic instability is suppressed in the region. The irregular variations of the KE transfers leads to a weak seasonal cycle of the regional submesoscale turbulence.
- In the deep basin of the eastern GoM, the submesoscale KE is larger in winter than in summer. The prevalent winter KE reservoir is fueled by strong conversion of energy from the APE reservoir (i.e., buoyancy conversion), which is maintained by forward APE cascades to the submesoscales, processes of dominant baroclinic instability. Interestingly, a spatially coherent pool of inverse KE cascade from the submesoscales to the background flow is found in the northern tip of the LC, which serves as the major sink for winter submesoscale KE. The intensities of the energetics are considerably weaker in summer, during which the leading source of submesoscale KE is from wind forcing instead of buoyancy conversion due to the shallow mixed layer and weak frontogenesis during this period of the year.
- In the northern GoM, a similar winter maximum is observed but with a much larger amplitude compared to that in the deep basin. The dominant source for the submesoscale KE during winter is from buoyancy conversion, and to a lesser extent from forward KE cascades from the mesoscales. To maintain the balance, the excess submesoscale KE must be dissipated locally (since nonlocal advection is negligible), implying a forward cascade of KE en route to finescale dissipation (Müller et al. 2005; Capet et al. 2008b; Molemaker et al. 2010), although a simulation with much higher resolution would be required to explicitly diagnose such a forward cascade. Different from the other two subdomains, there is a prevalent winter generation of submesoscale APE via buoyancy forcing, which is nearly balanced by the apparent APE sink due to the nonlinearity of the reference stratification. During the summer months, the submesoscale KE is dominantly generated by episodic tropical storm/hurricane winds, and dissipated through inverse KE cascade toward the mesoscales.

This study provides a first attempt in describing the spatial and temporal characteristics of the energy cascades and pathways associated with submesoscale currents in the eastern GoM. An important message from those feature-rich maps of energetics is that whether the submesoscale flows are efficient conduits to cascade KE of the large-scale circulation to dissipation scales is region and time dependent. Our formalism can be applied to other regional or global oceans to study the scale interactions, flow instabilities and energy pathways. It should be noted that unbalanced wave motions (e.g., internal gravity waves) are not considered in the present study. More work is required to unravel the geophysical distribution and temporal variation of the interactions between these unbalanced waves and balanced submesoscale and mesoscale motions.

A limitation of this study is that the present 1/48° simulation does not resolve submesoscale motions below ~10 km, which is the effective midlatitude resolution of the llc4320 simulation (Su et al. 2018). This marginal resolution could impact the submesoscale energetics, especially those during summer when the typical length of the submesoscale motions goes below the grid scale. An example is provided by Barkan et al. (2017) who found that submesoscale-relevant quantities across different resolutions show no sign of convergence, even with 150-m horizontal grid spacing. This raises an extremely challenging issue for models to capture the full range of submesoscale motions.

Another limitation of the present study is that the APE definition employed in this study is from Lorenz (1955) and, essentially, carries a quasigeostrophic (QG) assumption. The QG APE takes a quadratic form which is needed to obtain a physically meaningful multiscale APE expression and associated canonical APE transfer analogous to that for KE (see Liang 2016 for a comprehensive derivation). However, this definition assumes that the density perturbation is small compared with the reference stratification. We are aware that this could be problematic in the submesoscale-active mixed layer where the density perturbation could be exceptionally large. For arbitrary stratifications, a more general nonquadratic APE definition should be adapted, such as the one proposed by Holliday and McIntyre (1981). How to express a nonquadratic energy, i.e., a nonquadratic norm, in a function subspace (here multiscale window), and how to derive its associated canonical transfers and other energetics, requires much additional work in functional analysis. This type of analysis is left for future studies.

Acknowledgments. The authors thank Dhruv Balwada and an anonymous referee for their valuable comments. The llc4320

model output used in this study is available online (https://data.nas.nasa.gov/ecco/data.php?dir=/eccodata/llc_4320). YY thanks Jihai Dong for helping to access the model output. YY and XSL are supported by the National Science Foundation of China (NSFC) under Grants 41806023 and 41975064, 2015 Jiangsu Program of Entrepreneurship and Innovation Group, NUIST Startup Program (2017r054), Natural Science Foundation of the Higher Education Institutions of Jiangsu Province (18KJB170019), and the CSC–SOA Joint Scholarship Program (201804180031). JCM is supported by the Gulf of Mexico Research Institute (S1539-664390-UCLA). RHW and YL are partially supported by the National Academies of Sciences, Engineering and Medicine (NASEM) UGOS-1 (2000009918) and the NOAA IOOS SECOORA Program (NA16NOS0120028). HZ and DM carried research at the Jet Propulsion Laboratory, California Institute of Technology, under contract with NASA, with support from the Physical Oceanography (PO) and Modeling, Analysis, and Prediction (MAP) Programs.

REFERENCES

Aluie, H., M. Hecht, and G. K. Vallis, 2018: Mapping the energy cascade in the North Atlantic Ocean: The coarse-graining approach. *J. Phys. Oceanogr.*, **48**, 225–244, https://doi.org/10.1175/JPO-D-17-0100.1.

Balwada, D., J. H. LaCasce, and K. G. Speer, 2016: Scale-dependent distribution of kinetic energy from surface drifters in the Gulf of Mexico. *Geophys. Res. Lett.*, **43**, 10 856–10 863, https://doi.org/10.1002/2016GL069405.

Barkan, R., K. B. Winters, and S. G. Llewellyn Smith, 2015: Energy cascades and loss of balance in a reentrant channel forced by wind stress and buoyancy fluxes. *J. Phys. Oceanogr.*, **45**, 272–293, https://doi.org/10.1175/JPO-D-14-0068.1.

——, J. C. McWilliams, A. F. Shchepetkin, M. J. Molemaker, L. Renault, A. Bracco, and J. Choi, 2017: Submesoscale dynamics in the northern Gulf of Mexico. Part I: Regional and seasonal characterization and the role of river outflow. *J. Phys. Oceanogr.*, **47**, 2325–2346, https://doi.org/10.1175/JPO-D-17-0035.1.

——, M. J. Molemaker, K. Srinivasan, J. C. McWilliams, and E. A. D'Asaro, 2019: The role of horizontal divergence in submesoscale frontogenesis. *J. Phys. Oceanogr.*, **49**, 1593–1618, https://doi.org/10.1175/JPO-D-18-0162.1.

Beron-Vera, F. J., and J. H. LaCasce, 2016: Statistics of simulated and observed pair separations in the Gulf of Mexico. *J. Phys. Oceanogr.*, **46**, 2183–2199, https://doi.org/10.1175/JPO-D-15-0127.1.

Boccaletti, G., R. Ferrari, and B. Fox-Kemper, 2007: Mixed layer instabilities and restratification. *J. Phys. Oceanogr.*, **37**, 2228–2250, https://doi.org/10.1175/JPO3101.1.

Bracco, A., J. Choi, K. Joshi, H. Luo, and J. C. McWilliams, 2016: Submesoscale currents in the northern Gulf of Mexico: Deep phenomena and dispersion over the continental slope. *Ocean Modell.*, **101**, 43–58, https://doi.org/10.1016/j.ocemod.2016.03.002.

Brüggemann, N., and C. Eden, 2015: Routes to dissipation under different dynamical conditions. *J. Phys. Oceanogr.*, **45**, 2149–2168, https://doi.org/10.1175/JPO-D-14-0205.1.

Callies, J., R. Ferrari, J. M. Klymak, and J. Gula, 2015: Seasonality in submesoscale turbulence. *Nat. Commun.*, **6**, 6862, https://doi.org/10.1038/ncomms7862.

——, R. Barkan, and A. N. Garabato, 2020: Time scales of submesoscale flow inferred from a mooring array. *J. Phys. Oceanogr.*, **50**, 1065–1086, https://doi.org/10.1175/JPO-D-19-0254.1.

Capet, X., P. Klein, B. L. Hua, G. Lapeyre, and J. C. McWilliams, 2008a: Surface kinetic energy transfer in surface quasi-geostrophic flows. *J. Fluid Mech.*, **604**, 165–174, https://doi.org/10.1017/S0022112008001110.

——, J. C. McWilliams, M. J. Molemaker, and A. F. Shchepetkin, 2008b: Mesoscale to submesoscale transition in the California Current System. Part III: Energy balance and flux. *J. Phys. Oceanogr.*, **38**, 2256–2269, https://doi.org/10.1175/2008JPO3810.1.

——, ——, ——, and ——, 2008c: Mesoscale to submesoscale transition in the California Current System. Part II: Frontal processes. *J. Phys. Oceanogr.*, **38**, 44–64, https://doi.org/10.1175/2007JPO3672.1.

——, G. Roullet, P. Klein, and G. Maze, 2016: Intensification of upper-ocean submesoscale turbulence through Charney baroclinic instability. *J. Phys. Oceanogr.*, **46**, 3365–3384, https://doi.org/10.1175/JPO-D-16-0050.1.

Charney, J. G., 1971: Geostrophic turbulence. *J. Atmos. Sci.*, **28**, 1087–1095, https://doi.org/10.1175/1520-0469(1971)028<1087:GT>2.0.CO;2.

D'Asaro, E., C. Lee, L. Rainville, R. Harcourt, and L. Thomas, 2011: Enhanced turbulence and energy dissipation at ocean fronts. *Science*, **332**, 318–322, https://doi.org/10.1126/science.1201515.

de Boyer Montégut, C., G. Madec, A. S. Fischer, A. Lazar, and D. Iudicone, 2004: Mixed layer depth over the global ocean: An examination of profile data and a profile-based climatology. *J. Geophys. Res.*, **109**, C12003, https://doi.org/10.1029/2004JC002378.

Dong, J., B. Fox-Kemper, H. Zhang, and C. Dong, 2020: The seasonality of submesoscale energy production, content, and cascade. *Geophys. Res. Lett.*, **47**, e2020GL087388, https://doi.org/10.1029/2020GL087388.

Donohue, K. A., D. R. Watts, P. Hamilton, R. Leben, and M. Kennelly, 2016: Loop Current Eddy formation and baroclinic instability. *Dyn. Atmos. Oceans*, **76**, 195–216, https://doi.org/10.1016/j.dynatmoce.2016.01.004.

Fox-Kemper, B., R. Ferrari, and R. Hallberg, 2008: Parameterization of mixed layer eddies. Part I: Theory and diagnosis. *J. Phys. Oceanogr.*, **38**, 1145–1165, https://doi.org/10.1175/2007JPO3792.1.

Gula, J., M. J. Molemaker, and J. C. McWilliams, 2014: Submesoscale cold filaments in the Gulf Stream. *J. Phys. Oceanogr.*, **44**, 2617–2643, https://doi.org/10.1175/JPO-D-14-0029.1.

——, ——, and ——, 2016: Topographic generation of submesoscale centrifugal instability and energy dissipation. *Nat. Commun.*, **7**, 12811, https://doi.org/10.1038/ncomms12811.

Hamilton, P., A. Lugo-Fernández, and J. Sheinbaum, 2016: A Loop Current experiment: Field and remote measurements. *Dyn. Atmos. Oceans*, **76**, 156–173, https://doi.org/10.1016/j.dynatmoce.2016.01.005.

——, A. Bower, H. Furey, R. Leben, and P. Pérez-Brunius, 2019: The loop current: Observations of deep eddies and topographic waves. *J. Phys. Oceanogr.*, **49**, 1463–1483, https://doi.org/10.1175/JPO-D-18-0213.1.

Harrison, D. E., and A. R. Robinson, 1978: Energy analysis of open regions of turbulent flows—Mean eddy energetics of a numerical ocean circulation experiment. *Dyn. Atmos. Oceans*, **2**, 185–211, https://doi.org/10.1016/0377-0265(78)90009-X.

Holliday, D., and M. E. McIntyre, 1981: On potential energy density in an incompressible, stratified fluid. *J. Fluid Mech.*, **107**, 221–225, https://doi.org/10.1017/S0022112081001742.

Holopainen, E. O., 1978: A diagnostic study of the kinetic energy balance of the long-term mean flow and the associated transient fluctuations in the atmosphere. *Geophysica*, **15**, 125–145.

Hoskins, B. J., 1982: The mathematical theory of frontogenesis. *Annu. Rev. Fluid Mech.*, **14**, 131–151, https://doi.org/10.1146/annurev.fl.14.010182.001023.

Kang, D., and E. N. Curchitser, 2017: On the evaluation of seasonal variability of the ocean kinetic energy. *J. Phys. Oceanogr.*, **47**, 1675–1683, https://doi.org/10.1175/JPO-D-17-0063.1.

Klein, P., and G. Lapeyre, 2009: The oceanic vertical pump induced by mesoscale and submesoscale turbulence. *Annu. Rev. Mar. Sci.*, **1**, 351–375, https://doi.org/10.1146/annurev.marine.010908.163704.

——, B. L. Hua, G. Lapeyre, X. Capet, S. Le Gentil, and H. Sasaki, 2008: Upper ocean turbulence from high-resolution 3D simulations. *J. Phys. Oceanogr.*, **38**, 1748–1763, https://doi.org/10.1175/2007JPO3773.1.

Kolmogorov, A. N., V. Levin, J. C. R. Hunt, O. M. Phillips, and D. Williams, 1991: Dissipation of energy in the locally isotropic turbulence. *Proc. Roy. Soc. London*, **434A**, 15–17, https://doi.org/10.1098/rspa.1991.0076.

Lévy, M., D. Iovino, L. Resplandy, P. Klein, G. Madec, A.-M. Tréguier, S. Masson, and K. Takahashi, 2012: Large-scale impacts of submesoscale dynamics on phytoplankton: Local and remote effects. *Ocean Modell.*, **43–44**, 77–93, https://doi.org/10.1016/j.ocemod.2011.12.003.

Liang, X. S., 2016: Canonical transfer and multiscale energetics for primitive and quasigeostrophic atmospheres. *J. Atmos. Sci.*, **73**, 4439–4468, https://doi.org/10.1175/JAS-D-16-0131.1.

——, and A. R. Robinson, 2005: Localized multiscale energy and vorticity analysis: I. Fundamentals. *Dyn. Atmos. Oceans*, **38**, 195–230, https://doi.org/10.1016/j.dynatmoce.2004.12.004.

——, and D. G. M. Anderson, 2007: Multiscale window transform. *Multiscale Model. Simul.*, **6**, 437–467, https://doi.org/10.1137/06066895X.

——, and A. R. Robinson, 2007: Localized multi-scale energy and vorticity analysis: II. Finite-amplitude instability theory and validation. *Dyn. Atmos. Oceans*, **44**, 51–76, https://doi.org/10.1016/j.dynatmoce.2007.04.001.

——, and ——, 2009: Multiscale processes and nonlinear dynamics of the circulation and upwelling events off Monterey Bay. *J. Phys. Oceanogr.*, **39**, 290–313, https://doi.org/10.1175/2008JPO3950.1.

Liu, Y., R. H. Weisberg, C. Hu, and L. Zheng, 2011: Tracking the deepwater horizon oil spill: A modeling perspective. *Eos, Trans. Amer. Geophys. Union*, **92**, 45–46, https://doi.org/10.1029/2011EO060001.

——, ——, S. Vignudelli, and G. T. Mitchum, 2016: Patterns of the loop current system and regions of sea surface height variability in the eastern Gulf of Mexico revealed by the self-organizing maps. *J. Geophys. Res.*, **121**, 2347–2366, https://doi.org/10.1002/2015JC011493.

Lorenz, E. N., 1955: Available potential energy and the maintenance of the general circulation. *Tellus*, **7**, 157–167, https://doi.org/10.3402/tellusa.v7i2.8796.

Luo, H., A. Bracco, Y. Cardona, and J. C. McWilliams, 2016: Submesoscale circulation in the northern Gulf of Mexico: Surface processes and the impact of the freshwater river input. *Ocean Modell.*, **101**, 68–82, https://doi.org/10.1016/j.ocemod.2016.03.003.

Ma, J., and X. S. Liang, 2017: Multiscale dynamical processes underlying the wintertime Atlantic blockings. *J. Atmos. Sci.*, **74**, 3815–3831, https://doi.org/10.1175/JAS-D-16-0295.1.

Marshall, J., A. Adcroft, C. Hill, L. Perelman, and C. Heisey, 1997: A finite-volume, incompressible Navier Stokes model for studies of the ocean on parallel computers. *J. Geophys. Res.*, **102**, 5753–5766, https://doi.org/10.1029/96JC02775.

McWilliams, J. C., 2016: Submesoscale currents in the ocean. *Proc. Roy. Soc.*, **472A**, 20160117, https://doi.org/10.1098/rspa.2016.0117.

——, 2017: Submesoscale surface fronts and filaments: Secondary circulation, buoyancy flux, and frontogenesis. *J. Fluid Mech.*, **823**, 391–432, https://doi.org/10.1017/jfm.2017.294.

Menemenlis, D., J. Campin, P. Heimbach, C. Hill, T. Lee, A. Nguyen, M. Schodlok, and H. Zhang, 2008: ECCO2: High resolution global ocean and sea ice data synthesis. *Mercator Ocean Quarterly Newsletter*, No. 31, Mercator Ocean, Ramonville-Saint-Agne, France, 13–21.

Mensa, J. A., Z. Garraffo, A. Griffa, T. M. Özgökmen, A. Haza, and M. Veneziani, 2013: Seasonality of the submesoscale dynamics in the Gulf Stream region. *Ocean Dyn.*, **63**, 923–941, https://doi.org/10.1007/s10236-013-0633-1.

Molemaker, M. J., and J. C. McWilliams, 2010: Local balance and cross-scale flux of available potential energy. *J. Fluid Mech.*, **645**, 295–314, https://doi.org/10.1017/S0022112009992643.

——, ——, and X. Capet, 2010: Balanced and unbalanced routes to dissipation in an equilibrated Eady flow. *J. Fluid Mech.*, **654**, 35–63, https://doi.org/10.1017/S0022112009993272.

Müller, P., J. McWilliams, and J. Molemaker, 2005: Routes to dissipation in the ocean: The 2D/3D turbulence conundrum. *Marine Turbulence: Theories, Observations and Models*, H. Baumert, J. Simpson, and J. Sundermann, Eds., Cambridge University Press, 397–405.

Pedlosky, J., 1987: *Geophysical Fluid Dynamics*. 2nd ed. Springer-Verlag, 710 pp.

Plumb, R. A., 1983: A new look at the energy cycle. *J. Atmos. Sci.*, **40**, 1669–1688, https://doi.org/10.1175/1520-0469(1983)040<1669:ANLATE>2.0.CO;2.

Poje, A. C., and Coauthors, 2014: Submesoscale dispersion in the vicinity of the Deepwater Horizon spill. *Proc. Natl. Acad. Sci. USA*, **111**, 12 693–12 698, https://doi.org/10.1073/pnas.1402452111.

——, T. M. Özgökmen, D. J. Bogucki, and A. D. Kirwan, 2017: Evidence of a forward energy cascade and Kolmogorov self-similarity in submesoscale ocean surface drifter observations. *Phys. Fluids*, **29**, 020701, https://doi.org/10.1063/1.4974331.

Qiu, B., S. Chen, P. Klein, H. Sasaki, and Y. Sasai, 2014: Seasonal mesoscale and submesoscale eddy variability along the North Pacific Subtropical Countercurrent. *J. Phys. Oceanogr.*, **44**, 3079–3098, https://doi.org/10.1175/JPO-D-14-0071.1.

——, ——, ——, J. Wang, H. Torres, L.-L. Fu, and D. Menemenlis, 2018: Seasonality in transition scale from balanced to unbalanced motions in the World Ocean. *J. Phys. Oceanogr.*, **48**, 591–605, https://doi.org/10.1175/JPO-D-17-0169.1.

Rocha, C. B., S. T. Gille, T. K. Chereskin, and D. Menemenlis, 2016: Seasonality of submesoscale dynamics in the Kuroshio Extension. *Geophys. Res. Lett.*, **43**, 2016GL071349, https://doi.org/10.1002/2016GL071349.

Salmon, R., 1980: Baroclinic instability and geostrophic turbulence. *Geophys. Astrophys. Fluid Dyn.*, **15**, 167–211, https://doi.org/10.1080/03091928008241178.

Saltsman, B., 1957: Equations governing the energetics of the larger scales of atmospheric turbulence in the domain of wave number. *J. Meteor.*, **14**, 513–523, https://doi.org/10.1175/1520-0469(1957)014<0513:EGTEOT>2.0.CO;2.

Sasaki, H., P. Klein, B. Qiu, and Y. Sasai, 2014: Impact of oceanic-scale interactions on the seasonal modulation of ocean dynamics by the atmosphere. *Nat. Commun.*, **5**, 5636, https://doi.org/10.1038/ncomms6636.

Savage, A. C., and Coauthors, 2017: Spectral decomposition of internal gravity wave sea surface height in global models. *J. Geophys. Res. Oceans*, **122**, 7803–7821, https://doi.org/10.1002/2017JC013009.

Schubert, R., J. Gula, R. J. Greatbatch, B. Baschek, and A. Biastoch, 2020: The submesoscale kinetic energy cascade: Mesoscale absorption of submesoscale mixed layer eddies and frontal downscale fluxes. *J. Phys. Oceanogr.*, **50**, 2573–2589, https://doi.org/10.1175/JPO-D-19-0311.1.

Scott, R. B., and F. Wang, 2005: Direct evidence of an oceanic inverse kinetic energy cascade from satellite altimetry. *J. Phys. Oceanogr.*, **35**, 1650–1666, https://doi.org/10.1175/JPO2771.1.

Siegelman, L., 2020: Energetic submesoscale dynamics in the ocean interior. *J. Phys. Oceanogr.*, **50**, 727–749, https://doi.org/10.1175/JPO-D-19-0253.1.

Skyllingstad, E. D., and R. M. Samelson, 2012: Baroclinic frontal instabilities and turbulent mixing in the surface boundary layer. Part I: Unforced simulations. *J. Phys. Oceanogr.*, **42**, 1701–1716, https://doi.org/10.1175/JPO-D-10-05016.1.

Srinivasan, K., J. C. McWilliams, L. Renault, H. G. Hristova, J. Molemaker, and W. S. Kessler, 2017: Topographic and mixed layer submesoscale currents in the near-surface southwestern tropical Pacific. *J. Phys. Oceanogr.*, **47**, 1221–1242, https://doi.org/10.1175/JPO-D-16-0216.1.

Su, Z., J. Wang, P. Klein, A. F. Thompson, and D. Menemenlis, 2018: Ocean submesoscales as a key component of the global heat budget. *Nat. Commun.*, **9**, 775, https://doi.org/10.1038/s41467-018-02983-w.

Thomas, L. N., A. Tandon, and A. Mahadevan, 2013: Submesoscale processes and dynamics. *Ocean Modeling in an Eddying Regime*, *Geophys. Monogr.*, Vol. 177, Amer. Geophys. Union, 17–38.

Thompson, A. F., A. Lazar, C. Buckingham, A. C. Naveira Garabato, G. M. Damerell, and K. J. Heywood, 2016: Open-Ocean submesoscale motions: A full seasonal cycle of mixed layer instabilities from gliders. *J. Phys. Oceanogr.*, **46**, 1285–1307, https://doi.org/10.1175/JPO-D-15-0170.1.

Uchida, T., D. Balwada, R. Abernathey, G. McKinley, S. Smith, and M. Lévy, 2019: The contribution of submesoscale over mesoscale eddy iron transport in the open southern ocean. *J. Adv. Model. Earth Syst.*, **11**, 3934–3958, https://doi.org/10.1029/2019MS001805.

von Storch, J.-S., C. Eden, I. Fast, H. Haak, D. Hernández-Deckers, E. Maier-Reimer, J. Marotzke, and D. Stammer, 2012: An estimate of the Lorenz energy cycle for the World Ocean based on the STORM/NCEP simulation. *J. Phys. Oceanogr.*, **42**, 2185–2205, https://doi.org/10.1175/JPO-D-12-079.1.

Wang, S., Z. Jing, H. Liu, and L. Wu, 2018: Spatial and seasonal variations of submesoscale eddies in the eastern tropical Pacific Ocean. *J. Phys. Oceanogr.*, **48**, 101–116, https://doi.org/10.1175/JPO-D-17-0070.1.

Weisberg, R. H., Z. Li, and F. Muller-Karger, 2001: West Florida shelf response to local wind forcing: April 1998. *J. Geophys. Res.*, **106**, 31 239–31 262, https://doi.org/10.1029/2000JC000529.

Xu, F., and X. S. Liang, 2017: On the generation and maintenance of the 2012/13 sudden stratospheric warming. *J. Atmos. Sci.*, **74**, 3209–3228, https://doi.org/10.1175/JAS-D-17-0002.1.

Yang, Y., R. H. Weisberg, Y. Liu, and X. San Liang, 2020: Instabilities and multiscale interactions underlying the loop current eddy shedding in the Gulf of Mexico. *J. Phys. Oceanogr.*, **50**, 1289–1317, https://doi.org/10.1175/JPO-D-19-0202.1.

Zhang, Z., Y. Zhang, B. Qiu, H. Sasaki, Z. Sun, X. Zhang, W. Zhao, and J. Tian, 2020: Spatiotemporal characteristics and generation mechanisms of submesoscale currents in the northeastern South China Sea revealed by numerical simulations. *J. Geophys. Res. Oceans*, **125**, e2019JC015404, https://doi.org/10.1029/2019JC015404.

Zhao, Y.-B., and X. S. Liang, 2018: On the inverse relationship between the boreal wintertime Pacific Jet strength and storm-track intensity. *J. Climate*, **31**, 9545–9564, https://doi.org/10.1175/JCLI-D-18-0043.1.

Zhong, Y., and A. Bracco, 2013: Submesoscale impacts on horizontal and vertical transport in the Gulf of Mexico. *J. Geophys. Res. Oceans*, **118**, 5651–5668, https://doi.org/10.1002/jgrc.20402.